Epitaxial Growth of Molecular Crystals on van der Waals Substrates for High-Performance Organic Electronics

Chul-Ho Lee, Theanne Schiros, Elton J. G. Santos, Bumjung Kim, Kevin G. Yager, Seok Ju Kang, Sunwoo Lee, Jaeeun Yu, Kenji Watanabe, Takashi Taniguchi, James Hone, Efthimios Kaxiras, Colin Nuckolls, and Philip Kim**

The growth of high-quality organic semiconductors on supporting substrates with minimal disorder is the key requirement for realizing high-performance organic electronics.[1,2] However, the absence of an epitaxial relation and the presence of disorder make it particularly challenging to grow high-quality organic crystals having few defects and grain boundaries on conventional insulating substrates.[3,4] Here, we report epitaxial growth of highly ordered, crystalline organic films on van der Waals (vdW) substrates and demonstrate high carrier mobility comparable to those of single-crystal counterparts.[5] High-quality rubrene films with large single-crystalline domains were grown on hexagonal boron nitride (h-BN) layers with an in-plane crystallographic registry. Furthermore, using graphene as the vdW electrical contacts, high field-effect mobility (11.5 $cm^2 V^{-1} s^{-1}$) was achieved, attributable to an atomically sharp interface with low charge trap density between rubrene and h-BN. The ability to grow high-quality organic/inorganic epitaxial vdW heterostructures, combined with recent progress on large-area growth of layered materials,[6,7] provides new opportunities for the scalable fabrication of high-performance organic electronic devices.

Controlling the interface between organic films and inorganic substrates is of crucial importance for organic electronic applications, because this interface governs the initial nucleation during the growth of molecular films as well as the field-induced charge-carrier transport.[2,8–10] In particular, charge transport is affected greatly by interfacial disorder, such as surface roughness and charge traps, as well as structural disorder of the molecular materials at the interface.[9,11–14] The highest carrier mobility and intrinsic band-like transport have been achieved mostly with organic single crystals grown by a physical vapor transport method and assembled onto surface-functionalized device structures or suspended over an "air-gap".[15,16] Although this approach provides a platform for fundamental transport studies, the complicated device geometry and fabrication processes prevent its practical implementation. Therefore, it is desirable to grow high-quality crystalline films directly on functional substrates.[17–20] However, device performance comparable with that of free-standing single-crystal devices has not been achieved due to the difficulty in forming organic films with long-range structural ordering on typical substrates such as silicon oxide, glass and plastic, which possess a high degree of disorder.

Unlike amorphous substrates, two-dimensional (2D) dielectric materials such as h-BN and other vdW materials such as metal oxides and metal chalcogenides offer a new type of substrate for high-quality epitaxial growth of organic semiconductor films. In general, the 2D crystal lattice of layered materials should allow organic molecules to assemble into well-ordered structures via vdW interactions while minimizing random heterogeneous nucleation processes.[3] In addition, a vdW surface is free of dangling bonds and charge traps and thus enables the formation of the atomically well-defined interface with organic materials.[21] Reducing the density of the charge traps and/or scattering centers is desirable for high-performance devices.

In this study, we demonstrate the growth of high-quality rubrene crystals on exfoliated h-BN crystals. **Figure 1**a contains a schematic of a rubrene/h-BN heterostructure after crystal growth. It is important to note that the nonplanar molecular structure of rubrene favours assembly on the h-BN surface with an "edge-on"

Dr. C.-H. Lee, Prof. P. Kim
Department of Physics
Columbia University
New York, NY, 10027, USA
E-mail: pk2015@columbia.edu
Dr. C.-H. Lee, Dr. B. Kim,[+] Dr. S. J. Kang, J. Yu, Prof. C. Nuckolls
Department of Chemistry
Columbia University
New York, NY, 10027, USA
E-mail: cn37@columbia.edu
Dr. T. Schiros
Energy Frontier Research Center (EFRC)
Columbia University
New York, NY, 10027, USA
Dr. E. J. G. Santos, Prof. E. Kaxiras
School of Engineering and Applied Sciences and Department of Physics
Harvard University
Cambridge, MA, 02138
Dr. K. G. Yager
Center for Functional Nanomaterials
Brookhaven National Laboratory
Upton, NY, 11973, USA
S. Lee
Department of Electrical Engineering
Columbia University
New York, NY, 10027, USA
Dr. K. Watanabe, Dr. T. Taniguchi
Advanced Materials Laboratory
National Institute for Materials Science
1–1 Namiki, Tsukuba, 305–0044, Japan
Prof. J. Hone
Department of Mechanical Engineering
Columbia University
New York, NY, 10027, USA
[+]Present address: Department of Chemistry, New Jersey City University, Jersey City, NJ 07305, USA

DOI: 10.1002/adma.201304973

© 2014 WILEY-VCH Verlag GmbH & Co. KGaA, Weinheim

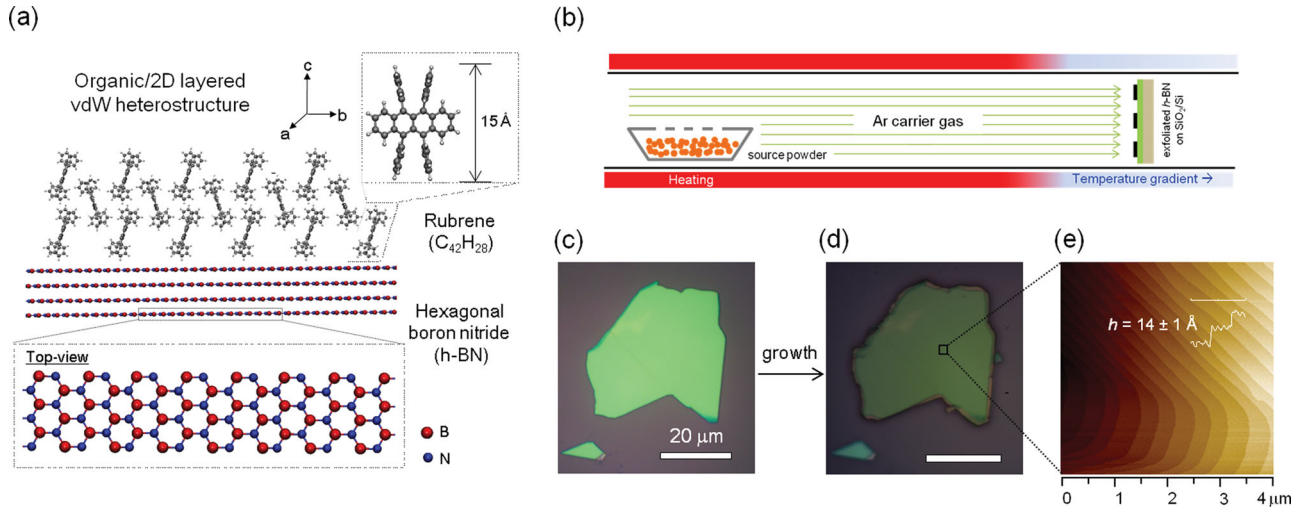

Figure 1. Growth of organic/2D layered vdW heterostructures. Schematic illustration of: a) the organic/2D layered vdW heterostructure composed of rubrene and h-BN and b) the vapor-phase transport method for the growth. Optical images of: c) the h-BN crystal exfoliated on a SiO_2/Si substrate and d) the rubrene film grown on h-BN. e) AFM image of the film surface and the height profile along the line. It shows a highly uniform terrace structure with the step height of 14 ± 1 Å.

orientation rather than "face-on" alignment. This arrangement offers an advantage for lateral charge transport parallel to the semiconductor/dielectric interface in a field-effect device geometry.[22,23] Figure 1b shows a schematic of the vapor-phase transport method used for the growth of rubrene crystals (see Experimental Section for details). To prepare the substrate for growth, we created thin layers of h-BN crystals that were mechanically exfoliated on SiO_2/Si substrates as shown in Figure 1c. Typically, single h-BN crystallites have a thickness of 10–60 nm and a lateral dimension larger than 10 μm. We chose high-quality crystallites that have extremely flat surfaces (roughness of less than 1 nm)[24] in order to provide atomically homogeneous substrate for the subsequent organic crystal growth. After cleaning the h-BN surface via thermal annealing, homogeneous rubrene films with thicknesses of 500–1000 nm were preferentially grown on the h-BN surface (Figure 1d) along with microcrystallites occasionally formed on the SiO_2 substrate at the optimal growth condition (see Supporting Information, Figure S1). The atomic force microscopy (AFM) image of the rubrene on h-BN shows atomically flat, highly uniform terraces with an average step height of 14 ± 1 Å (Figure 1e). The step height corresponds to the molecular length of the *c*-axis of rubrene.

Figure 2a shows a transmission electron microscopy (TEM) image and selected area electron diffraction (SAED) pattern of the rubrene film grown on an h-BN crystal. For this measurement, we place thin h-BN crystals on a holey TEM grid, and then grow the rubrene crystals. The rectangular diffraction patterns from rubrene (*hk*0) planes are clearly seen on top of the hexagonal diffraction patterns of h-BN $\{10\bar{1}0\}$ planes. The superposition of the two diffraction patterns without concentric rings clearly indicates that both h-BN and rubrene layers are crystalline and no amorphous layer is formed at the interface between the two crystals. Furthermore, by comparing the 2-fold diffraction pattern of rubrene to the 6-fold symmetric pattern of h-BN, we find that the two single crystals are rotated by an angle of ca. 4° between their *a*-axes.

Since SAED can only provide local structural information, we used grazing-angle X-ray diffraction (GIXD) with a synchrotron light source (Figure 2b). Due to the highly crystalline nature of the films, we observe sharp, intense, and well-defined Bragg diffraction peaks. Only a small fraction of the total diffraction peaks were observed at a given ϕ angle. The diffraction peaks appear and disappear over a narrow angular ϕ range (see Supporting Information, Figure S2). We thus obtain a complete reciprocal (*q*-space) diffraction pattern by measuring while the sample is rotated 360° around the film normal axis as shown in Figure 2c. The experimental data are in a good agreement with the computed diffraction patterns (indicated by green circles) from an orthorhombic unit cell with the lattice parameters (a = 7.19, b = 14.43, c = 26.83 Å).[25] This reveals *c*-axis-oriented growth of an orthorhombic rubrene crystal on the h-BN substrate. The lattice parameters obtained from GIXD are close to the values of a free-standing single crystal, indicating that the intermolecular interactions in our rubrene film are stronger than the interaction between the rubrene molecules and the h-BN substrate.[21]

The agreement between experimental and computational diffraction patterns enables a complete peak indexing and determination of in-plane crystallographic orientation of the rubrene film relative to the h-BN substrate. Figure 2d plots the intensity as a function of ϕ for a given diffraction peak. Interestingly, we find that rubrene crystals grown on h-BN have 6-fold symmetry even though the orthorhombic crystal structure of rubrene only has 2-fold symmetry. Considering that there is a possibility of multiple domains of rubrene on h-BN, the observed 6-fold GIXD suggests that the rubrene crystals as grown are epitaxially locked in the crystallographic direction of the 3-fold symmetric h-BN crystal. Furthermore, from the comparison between the measured GIXD patterns and the computed diffraction patterns for a series of ϕ angles, we extract the in-plane crystallographic relationship between *a*-axes of rubrene and h-BN with an offset of ca. 3° (see Supporting Information, Figure S2, S3), which is

© 2014 WILEY-VCH Verlag GmbH & Co. KGaA, Weinheim

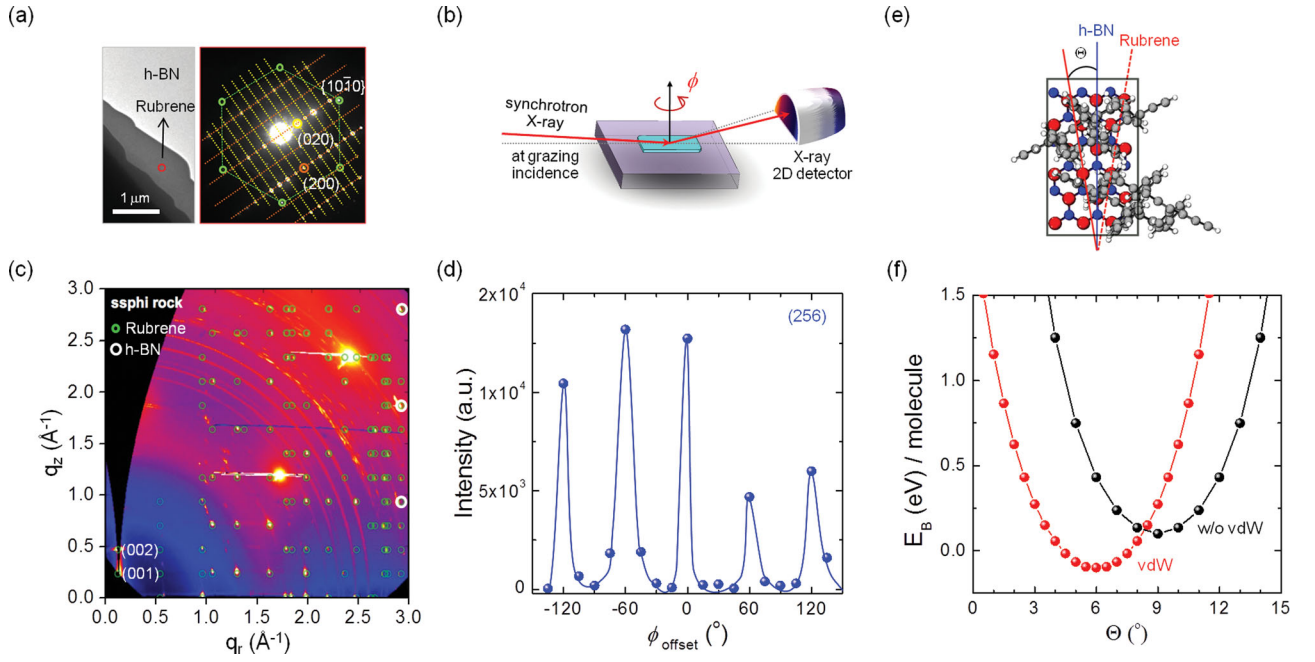

Figure 2. VdW epitaxial relation between rubrene and h-BN crystals. a) Bright-field TEM image and selected-area electron diffraction pattern of the rubrene crystal grown on h-BN. The rubrene (200), (020) and h-BN $\{10\bar{1}0\}$ planes are indicated by orange, yellow and green circles, respectively. b) Schematic of GIXD measurements. c) Measured and calculated 2D GIXD patterns of rubrene crystals grown on h-BN. Green and white circles represent the calculated diffraction patterns for orthorhombic rubrene and h-BN crystals, respectively. The two dominant bright features observed at the diffraction point, (q_r, q_z) ≈ (2.4 Å^{-1}, 2.5 Å^{-1}) and ≈ (1.2 Å^{-1}, 1.7 Å^{-1}) originate from the Si substrate underneath the thermally grown SiO_2 layer. d) Representative azimuthal (ϕ)-scan of GIXD for the (256) plane of rubrene, which shows the regular diffraction peaks with 6-fold symmetry. e) Top-view image of rubrene molecules on the h-BN surface using a ball-stick model. The black box defines the supercell used in the calculations with the definition of the in-plane misorientation angle (Θ). f) Plot of the binding energy per rubrene molecule as a function of Θ obtained from first-principles calculations. The red and black curves represent the calculations with and without vdW interactions, respectively.

similar to the ca. 4° offset observed in the SAED. It is interesting to note that despite the relatively weak molecule-substrate interactions that allow the structural parameters of the rubrene crystals on h-BN to be close to those of free-standing rubrene crystals, the interaction is strong enough to provide epitaxial registry between the two atomic lattices.

To further understand this epitaxial relation, we performed first-principles binding-energy calculations using density functional theory (see Experimental Section and Supporting Information for more details). We considered supercells composed of a single layer of the rubrene crystal on top of a h-BN layer at different in-plane misorientation angles (Θ) between the *a*-axes of rubrene and h-BN. Figure 2f shows the total energy per rubrene molecule as a function of Θ using two different density functionals with and without vdW interactions. In both cases, the minimum energy configuration is obtained when small misorientation angles of less than 10° are present. In particular, when vdW interactions are taken into account between rubrene and h-BN layers, the misorientation angle becomes even smaller to 6° and the system is more stabilized with reduction of energy by 0.20 eV per rubrene molecule. This agreement with experimental observations strongly suggests that a weak vdW interaction can still lead to epitaxial growth of rubrene crystals on h-BN substrates.

The vdW epitaxy of rubrene films allows us to achieve large single-crystalline domains on single-crystal h-BN. **Figure 3** displays a polarized optical microscopy image for a typical rubrene crystal grown on h-BN. The contrast in the polarized images at different angles is dependent on the in-plane crystallographic orientations due to the anisotropy of the rubrene crystal.[17] The domain size is determined by the size of the h-BN flakes, indicating that the rubrene is a single domain. The large single-domain growth of epitaxial films is critical to achieve intrinsic device characteristics with high carrier mobility, since grain boundaries can significantly decrease the mobility and thus deteriorate overall device performances.[26]

Figure 4 displays how we create field-effect device structures on these epitaxially grown rubrene crystals. Electrodes are required not only to contact the channel-dielectric interface between rubrene and h-BN where the hole accumulation layer is induced in our silicon back-gate devices, but also to provide a less disruptive surface for the crystal growth. We employ vdW graphene electrodes that serve as an electrical contact[27,28] as well as an epitaxial growth template.[23] Figure 4a shows a schematic diagram of the procedures of device fabrication. Prior to rubrene growth, chemical-vapor-deposited graphene films were transferred onto the top of h-BN layers using the pre-patterned poly-dimethyl siloxane (PDMS) stamp[27] to create a lateral graphene/h-BN/graphene heterostructure. During this transfer process, the h-BN surface over the channel region does not contact the PDMS and therefore remains clean, as confirmed by AFM imaging (Figure 4b). The separation between the two

© 2014 WILEY-VCH Verlag GmbH & Co. KGaA, Weinheim

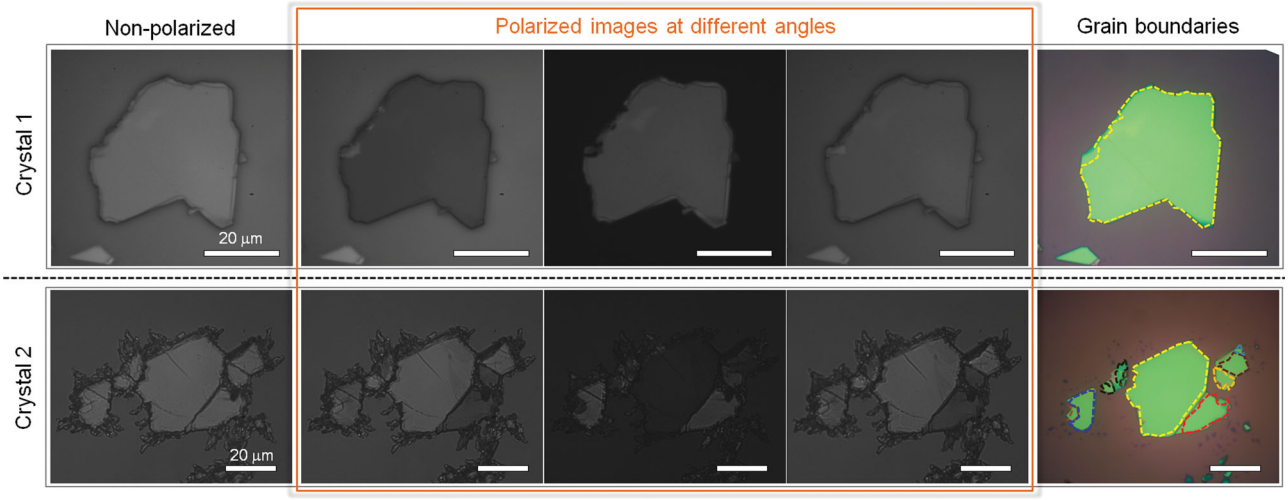

Figure 3. Rubrene crystalline films with large single-crystalline domains grown on h-BN. Polarization optical characterization for two representative samples. The normal (1st column) and polarized (2nd–4th columns) images at different angles are shown for each samples. The last column shows the grain map overlapped on the optical image of h-BN flakes. Crystal grains and grain boundaries are distinguished clearly by an optical contrast in polarized images and indicated by dashed lines with different colors in maps.

graphene electrodes, corresponding to the channel length, was 10 μm, and channel width determined by the width of the h-BN flakes was typically in the range of 10–30 μm.

Atomically thin graphene provides an optimal 2D morphology for the rubrene crystal growth on h-BN and is less disruptive to the surface than typical three-dimensional (3D) metal

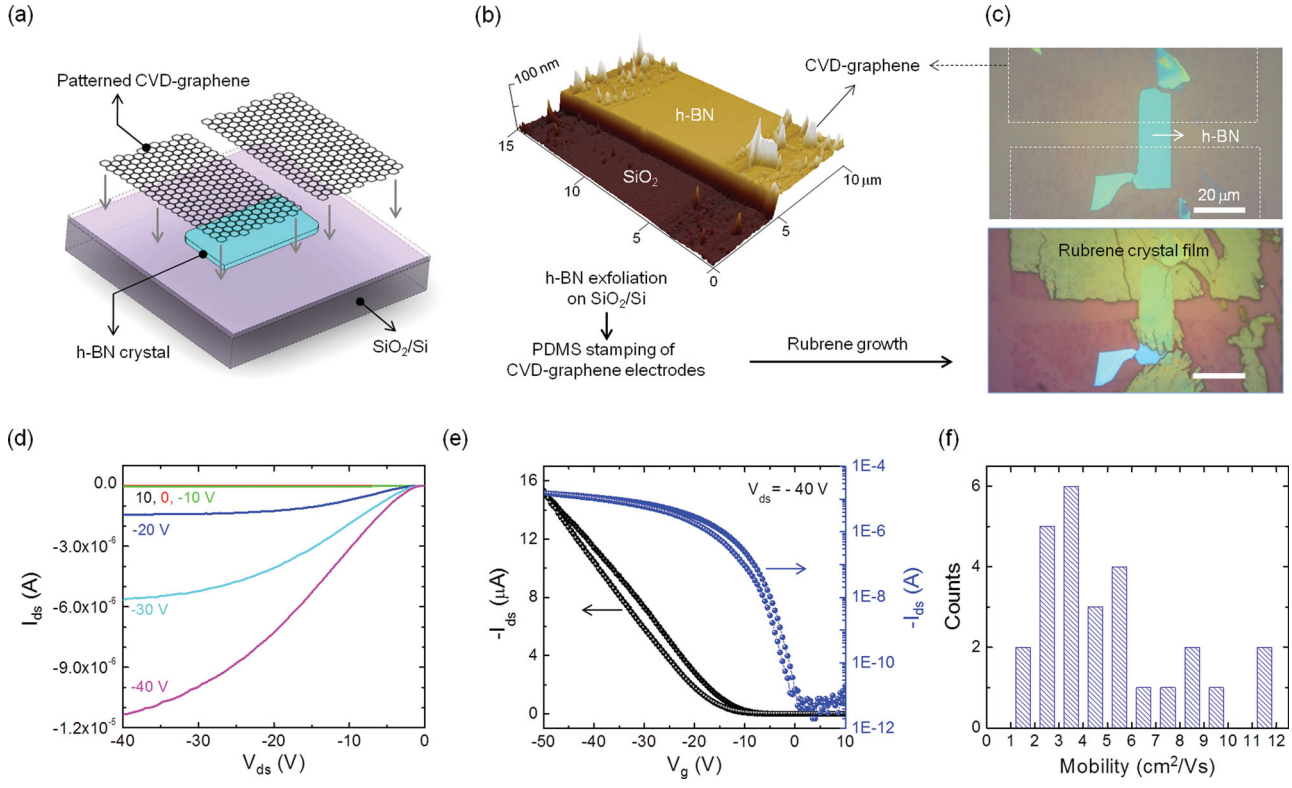

Figure 4. Fabrication and electrical characterization of FETs using graphene electrodes. a) Schematic illustration for the fabrication of graphene electrodes on h-BN. b) AFM image of the patterned CVD-graphene electrodes on the h-BN/SiO_2 substrate. c) Optical images of the device before (top) and after (bottom) rubrene crystal growth on the stacked graphene/h-BN structure. d,e) Representative output (d) and transfer (e) characteristic curves of FETs with graphene electrodes. f) Histogram of mobility measured from 27 devices. The average and maximum values of mobility are 5.1 ± 2.7 $cm^2 V^{-1} s^{-1}$ and 11.5 $cm^2 V^{-1} s^{-1}$, respectively.

© 2014 WILEY-VCH Verlag GmbH & Co. KGaA, Weinheim

electrodes. For example, when Au metal electrodes were used, small-domain polycrystalline films were grown on the contact area presumably due to random heterogeneous nucleation along the 3D edges as wells as lack of preferential assembly of molecules. This results in structural disorders such as grain boundaries that hindered carrier injection into the channel, causing extremely non-linear current–voltage curves with large contact resistances of a few hundred mega-ohms (see Supporting Information, Figure S4). In contrast, as shown in Figure 4c, the high-quality rubrene films were grown uniformly across the graphene/h-BN/graphene heterostructure where graphene only has an one-dimensional edge with the rubrene crystals. We also find that output characteristics of field-effect transistors (FETs) are significantly improved compared with those of the devices with metal electrodes. In particular, the series resistance at low source-drain bias (<1 V) was significantly reduced down to a few MΩ (Figure 4d), an improvement of two orders of magnitude when compared with Au electrodes. Note that the contact resistances (about several kΩ cm) are still high compared with those of single-crystal devices[29] because our epitaxial films can be structurally disordered in the vicinity of randomly stacked h-BN/graphene boundaries (see Supporting Information, Figure S5, S6).

The aforementioned, graphene-contacted, vdW heterostructured devices exhibited excellent device performances as organic transistors despite an imperfect contact. Figure 4e shows the transfer characteristic curves of FETs with negligibly small hysteresis and high on/off ratio of ca. 10^6, indicating very low density of deep-level trap states at the interface. In addition, field-effect mobility in the saturation regime[30] was substantially high; the average and maximum values were 5.1 ± 2.7 cm^2 V^{-1} s^{-1} and 11.5 cm^2 V^{-1} s^{-1}, respectively. Figure 4f shows a histogram of mobility measured from 27 devices. Note that the linear mobility was typically an order of magnitude lower (0.1–1 cm^2 V^{-1} s^{-1}) than the mobility we extracted from the saturation regime (see Supporting Information, Figure S6). Nevertheless, the highest mobility observed in these epitaxial vdW heterostructures is comparable to those of free-standing single crystals and represents a record for organic films grown on any substrates (see Supporting Information, Table S1). It should be also noted that the substantial variation in mobility could be attributed to the anisotropy of mobility according to epitaxial crystal orientations determined randomly by exfoliated h-BN crystals,[15] rather than grain boundaries that typically degrade carrier mobility by more than an order of magnitude.[26] All these device characteristics including negligible hysteresis and high mobility strongly support the formation of highly ordered crystalline films with an electrically clean semiconductor/dielectric interface that is consistent with our structural analyses.

In summary, we demonstrate that epitaxial vdW heterostructures of organic and vdW layered materials create high-performance organic electronic devices. High-quality rubrene films with large single-crystalline domains were grown on h-BN dielectric layers via vdW epitaxy. High carrier mobility comparable to free-standing single-crystal counterparts was achieved by forming interfacial electrical contacts with graphene electrodes. This highlights the advantages of heterostructured vdW dielectrics and contacts over commonly used materials to achieve high-performance organic electronic devices. More generally, the epitaxial approach to fabricate organic/inorganic vdW heterostructures can be readily expanded to numerous other organic and layered materials for various electronic and optoelectronic applications.

Experimental Section

Material Growth: Rubrene crystalline films were grown by a vapor-phase transport method. A source of rubrene powder (ca. 1 mg), which was purified two times, was placed in the sublimation zone at 230 °C. The SiO_2/Si substrate, on which h-BN flakes were exfoliated, was placed in the crystallization zone at 180 °C. Prior to the growth, the h-BN surface was cleaned via thermal annealing at 400 °C under vacuum (ca. 1 mTorr). AFM surface characterization after annealing reveals that we still have an atomically flat and clean substrate without much of damage or contamination. During the growth, the chamber was under vacuum (ca. 1 Torr), with flowing the high-purity argon gas (99.999%) as a carrier gas with the flow rate of 200 sccm. The growth was performed for 5 minutes, and then the system was cooled down slowly to room temperature.

Material Characterization: For the TEM measurements, rubrene films were grown directly on h-BN flakes suspended onto a copper TEM grid using a mechanical exfoliation method. Scanning-TEM images and SAED patterns were obtained at a low operation voltage of 80 kV to avoid the electron-beam damage with the TEM (JEOL, JEM-100CX). For the GIXD measurements, a single piece of an h-BN crystallite with the lateral dimensions larger than 100 μm was transferred onto a SiO_2/Si substrate using the PDMS stamping technique, and the rubrene crystals were grown the following the method described above. This allows us to obtain GIXD patterns from the rubrene films grown on a single crystallite of h-BN. The experiments were performed at the National Synchrotron Light Source (NSLS) of Brookhaven National Laboratory on the undulator-based X9 beam line, X-ray photons of 14.0 keV (0.08856 nm). The incident beam has a grazing incidence angle with the sample surface. The X-ray beam was focused to 100 μm in the horizontal and 50 μm in the vertical direction. The beam was aligned with the sample using a phosphor to calibrate beam position; the sample was laser-levelled to the in-plane rotation axis and rotated in 15° steps to determine in-plane registry with the underlying h-BN substrate. Additional details are provided in the Supporting Information.

First-Principles Calculations: The simulations reported here are based on density-functional-theory calculations using the SIESTA code.[31] The generalized gradient approximation[32] and nonlocal van der Waals density functional[33] was used together with double-ς plus polarized basis set, norm-conserving Troullier-Martins pseudopotentials[34] and a mesh cutoff of 150 Ry. We used a Fermi–Dirac distribution with an electronic temperature of $k_BT = 21$ meV. Additional details are provided in the Supporting Information.

Supporting Information

Supporting Information is available from the Wiley Online Library or from the author.

Acknowledgements

This work was supported as part of the Center for Re-defining Photovoltaic Efficiency Through Molecule Scale Control, an Energy Frontier Research Center funded by the U.S. Department of Energy, Office of Science, Office of Basic Energy Sciences under Award Number DE-SC0001085, and in part by the FAME Center, one of six centers of STARnet, a Semiconductor Research Corporation program sponsored by MARCO and DARPA. P.K. acknowledges the Nano Material Technology Development Program through the National Research Foundation

© 2014 WILEY-VCH Verlag GmbH & Co. KGaA, Weinheim

of Korea (NRF) funded by the Ministry of Science, ICT and Future Planning (2012M3A7B4049966). C.-H.L. acknowledges the Basic Science Research Program through the National Research Foundation of Korea (357–2011–1-C00035). GIXD measurements carried out in part at the Center for Functional Nanomaterials, and the National Synchrotron Light Source, Brookhaven National Laboratory, which are supported by the U.S. Department of Energy, Office of Basic Energy Sciences, under Contract No. DE-AC02–98CH10886. E.J.G.S. thanks the computational resources provided by the Extreme Science and Engineering Discovery Environment (XSEDE), supported by NSF grant numbers TG-DMR120049 and TG-PHY120021.

Received: October 6, 2013
Revised: November 24, 2013
Published online: January 23, 2014

[1] S. R. Forrest, *Chem. Rev.* **1997**, *97*, 1793.
[2] M. Eremtchenko, J. A. Schaefer, F. S. Tautz, *Nature* **2003**, *425*, 602.
[3] A. C. Hillier, M. D. Ward, *Phys. Rev. B* **1996**, *54*, 14037.
[4] D. E. Hooks, T. Fritz, M. D. Ward, *Adv. Mater.* **2001**, *13*, 227.
[5] R. W. I. de Boer, M. E. Gershenson, A. F. Morpurgo, V. Podzorov, *Phys. Status Solidi A* **2004**, *201*, 1302.
[6] S. Bae, H. Kim, Y. Lee, X. Xu, J.-S. Park, Y. Zheng, J. Balakrishnan, T. Lei, H. R. Kim, Y. I. Song, Y.-J. Kim, K. S. Kim, B. Özyilmaz, J.-H. Ahn, B. H. Hong, S. Iijima, *Nat. Nanotechnol.* **2010**, *5*, 574.
[7] L. Song, L. Ci, H. Lu, P. B. Sorokin, C. Jin, J. Ni, A. G. Kvashnin, D. G. Kvashnin, J. Lou, B. I. Yakobson, P. M. Ajayan, *Nano. Lett.* **2010**, *10*, 3209.
[8] F. Dinelli, M. Murgia, P. Levy, M. Cavallini, F. Biscarini, D. M. de Leeuw, *Phys. Rev. Lett.* **2004**, *92*, 116802.
[9] I. N. Hulea, S. Fratini, H. Xie, C. L. Mulder, N. N. Iossad, G. Rastelli, S. Ciuchi, A. F. Morpurgo, *Nat. Mater.* **2006**, *5*, 982.
[10] C. Stadler, S. Hansen, I. Kröger, C. Kumpf, E. Umbach, *Nat. Phys.* **2009**, *5*, 153.
[11] M. E. Gershenson, V. Podzorov, A. F. Morpurgo, *Rev. Mod. Phys.* **2006**, *78*, 973.
[12] V. Coropceanu, J. Cornil, D. A. da Silva Filho, Y. Olivier, R. Silbey, J. L. Brédas, *Chem. Rev.* **2007**, *107*, 926.
[13] M. F. Calhoun, C. Hsieh, V. Podzorov, *Phys. Rev. Lett.* **2007**, *98*, 096402.
[14] T. Vehoff, B. Baumeier, A. Troisi, D. Andrienko, *J. Am. Chem. Soc.* **2010**, *132*, 11702.
[15] V. C. Sundar, J. Zaumseil, V. Podzorov, E. Menard, R. L. Willett, T. Someya, M. E. Gershenson, J. A. Rogers, *Science* **2004**, *303*, 1644.
[16] N. A. Minder, S. Ono, Z. H. Chen, A. Facchetti, A. F. Morpurgo, *Adv. Mater.* **2012**, *24*, 503.
[17] N. Stingelin-Stutzmann, E. Smits, H. Wondergem, C. Tanase, P. Blom, P. Smith, D. De Leeuw, *Nat. Mater.* **2005**, *4*, 601.
[18] G. Giri, E. Verploegen, S. C. B. Mannsfeld, S. Atahan-Evrenk, D. H. Kim, S. Y. Lee, H. A. Becerril, A. Aspuru-Guzik, M. F. Toney, Z. Bao, *Nature* **2011**, *480*, 504.
[19] Y. Diao, B. C.-K. Tee, G. Giri, J. Xu, D. H. Kim, H. A. Becerril, R. M. Stoltenberg, T. H. Lee, G. Xue, S. C. B. Mannsfeld, Z. Bao, *Nat. Mater.* **2013**, *12*, 665.
[20] H. Y. Li, G. Giri, J. B.-H. Tok, Z. Bao, *MRS Bull.* **2013**, *38*, 34.
[21] A. Koma, *Thin Solid Films* **1992**, *216*, 72.
[22] H. Sirringhaus, P. J. Brown, R. H. Friend, M. M. Nielsen, K. Bechgaard, B. M. W. Langeveld-Voss, A. J. H. Spiering, R. A. J. Janssen, E. W. Meijer, P. Herwig, D. M. de Leeuw, *Nature* **1999**, *401*, 685.
[23] K. Xiao, W. Deng, J. K. Keum, M. Yoon, I. V. Vlassiouk, K. W. Clark, A.-P. Li, I. I. Kravchenko, G. Gu, E. A. Payzant, B. G. Sumpter, S. C. Smith, J. F. Browning, D. B. Geohegan, *J. Am. Chem. Soc.* **2013**, *135*, 3680.
[24] C. R. Dean, A. F. Young, I. Meric, C. Lee, L. Wang, S. Sorgenfrei, K. Watanabe, T. Taniguchi, P. Kim, K. L. Shepard, J. Hone, *Nat. Nanotechnol.* **2010**, *5*, 722.
[25] O. D. Jurchescu, A. Meetsma, T. T. M. Palstra, *Acta. Crystallogr. B* **2006**, *62*, 330.
[26] J. Rivnay, L. H. Jimison, J. E. Northrup, M. F. Toney, R. Noriega, S. Lu, T. J. Marks, A. Facchetti, A. Salleo, *Nat. Mater.* **2009**, *8*, 952.
[27] S. J. Kang, B. Kim, K. S. Kim, Y. Zhao, Z. Y. Chen, G. H. Lee, J. Hone, P. Kim, C. Nuckolls, *Adv. Mater.* **2011**, *23*, 3531.
[28] W. H. Lee, J. Park, S. H. Sim, S. Lim, K. S. Kim, B. H. Hong, K. Cho, *J. Am. Chem. Soc.* **2011**, *133*, 4447.
[29] I. N. Hulea, S. Russo, A. Molinari, A. F. Morpurgo, *Appl. Phys. Lett.* **2006**, *88*, 113512.
[30] The saturation mobility is estimated from $I_{ds} = (W/2L)C_g\mu(V_g - V_t)^2$, where W and L are the width and length of channel and $C_g\mu$, and V_t correspond to the capacitance of the gate dielectric, field-effect mobility and threshold voltage. In particular, we use the total thickness of h-BN (10–60 nm) and SiO_2 (280 nm) for the gate dielectric to calculate the capacitance because the dielectric constant of h-BN (3–4)[24] is almost same with that of SiO_2.
[31] J. M. Soler, E. Artacho, J. D. Gale, A. Garcia, J. Junquera, P. Ordejón, D. Sánchez-Portal, *J. Phys.: Condens. Matter* **2002**, *14*, 2745.
[32] J. P. Perdew, K. Burke, M. Ernzerhof, *Phys. Rev. Lett.* **1996**, *77*, 3865.
[33] M. Dion, H. Rydberg, E. Schröder, D. C. Langreth, B. I. Lundqvist, *Phys. Rev. Lett.* **2004**, *92*, 246401.
[34] N. Troullier, J. L. Martins, *Phys. Rev. B* **1991**, *43*, 1993.

© 2014 WILEY-VCH Verlag GmbH & Co. KGaA, Weinheim